nature geoscience

Article

https://doi.org/10.1038/s41561-023-01198-z

Fossil organic carbon utilization in marine Arctic fjord sediments by subsurface microorganisms

In the format provided by the authors and unedited

Supplement

Intact polar lipids source assignments

All three cores were dominated by phospholipids with variable relative amounts. While phosphatidylethanolamine (PE) and phosphatidylglycerol (PG) dominated the Brepollen long core HH14-897-GC-MF and the glacier-front core He560_26-2-K1, the marine influenced main basin core He519_2-3 contained higher amounts of phosphatidylcholine (PC), followed by PG and PE (Figure S 1). Phosphatidyl-(*N*)-monomethylethanolamine (PME), Phosphatidyl-(*N,N*)-dimethylethanolamine (PDME), diphosphatidylglycerol (DPG) and lyso-DPG were detected in minor amounts in all cores. The aminolipids, betaine lipids (BL), were also present in all three cores with varying amounts but always <10%. PG and PE are the most common lipids found in bacteria[1] and are typically assigned to sulfate-reducing bacteria[2,3] (with DPG) in marine sediments, although other gram-negative bacteria are also potential sources. The fatty acid distribution in PG, PE, and DPG support a bacterial source as $C_{16:1}$ fatty acids dominate these lipid classes as well as odd-numbered carbon fatty acids such as $C_{17:1}$ and $C_{br\text{-}15:0}$ (Figure S 2, note: the double bond and methyl-branch was not determined by HPLC-MS, but was identified by PLFA analyses via GC-MS). The assignment of PC to a bacterial source is not as straightforward as only 10% of all bacteria are estimated to possess the genes involved in its biosynthesis[4] and PC - with BL- is more commonly assigned to phytoplankton[5]. The higher abundance of PC in the marine-influenced core could point to detrital remains of phytoplankton, however, the fatty acid distribution indicates that a large part of PC is likely of bacterial origin (Figure S 2). Similarly, BL contain fatty acids that point to bacterial sources, but a small contribution from detrital sources that bypassed degradation in these organic-rich likely methanogenic anoxic sediments cannot be

excluded. It is to be expected that detrital contributions of phospholipids and betaine lipids decrease with sediment depth and age[6,7], however, it is possible that degradation in deeper methanogenic layers of organic rich sediments proceeds slower leading to a potential longer preservation of bacterial IPLs. The associated fatty acids $C_{16:1}$ and $C_{br\text{-}15:0}$ were chosen for compound specific radiocarbon analysis due to their predominant bacterial origin[8] and their abundance in the extracted IPL fractions. The different radiocarbon signatures of $C_{16:1}$ and $C_{br\text{-}15:0}$ fatty acids are likely due to different abundances in source bacteria, both in terms of fatty acid abundances within single organisms but also in the relative abundances of bacterial strains within the subsurface community. However, further microbiological methods like 16S RNA would be needed to address differences on a community level.

Compound specific radiocarbon dating of *n*-alkanes

n-Alkanes were separated from the neutral fraction of the intact polar lipid extract by a second silica column chromatography, eluting the alkane fraction with hexane. From three depth intervals of sediment core HH14-897-GC-MF, purified samples of *n*-C_{19}, *n*-C_{20}, *n*-C_{21}, and *n*-C_{22} as well as combined *n*-$C_{26+28+30}$ and *n*-$C_{27+29+31}$ were collected using the GC-PFC used similarly as for intact polar lipid fatty acid purification. The purified splits were radiocarbon dated in the same manner as the intact polar lipid fatty acids using AMS at the MICADAS facility of the Alfred-Wegener-Institute in Bremerhaven, Germany.

The radiocarbon values obtained for all *n*-alkane samples indicate that a large part of the organic matter is derived from a radiocarbon free source (Table S 1). The $F^{14}C$ values are close to the detection-limit for gas measurements and can be considered to be $F^{14}C=0$ within 2σ uncertainties in almost all cases except for the samples of combined *n*-$C_{27+29+31}$, whose $F^{14}C$ values suggest

minor contributions from younger materials (less than 3 % assuming a modern source)[9]. In combination with low CPI values (Figure S 3), the age of the *n*-alkanes supports the assumption that freshly synthesized OM from terrestrial vegetation contributes a negligible amount to sedimentary OM. These results further support the application of a two-endmember model for radiocarbon based isotopic mass balances calculations.

Sediment core age models

Core He519_2-3 (27 cm long) collected from the Hornsund fjord main basin revealed near-constant $^{210}Pb_{ex}$ in the topmost part, considered a surface mixed layer, and steadily decreasing activities below. The modeled accumulation rate is approximately 4.1 mm/yr. The isotope ^{137}Cs was detected throughout the core and its maximum may be related to the 1986 Chernobyl event. Due to deep sediment mixing, the age model can only be treated as an approximation, but all models confirm that the sediments are considerably younger than the ^{210}Pb extinction age and were deposited -or last mixed- within the era of artificial radionuclides (Figure S 4).

The longest core (154 cm) HH14-897-GC-MF was collected from an area in Brepollen that was deglaciated between 1936 and 1960. The $^{210}Pb_{ex}$ decreased with depth and revealed a rapid accumulation rate of approximately 147 mm/yr until around 1968, when the coring site was still close to the tidewater glacier termini, decreasing to approximately 8.1 mm/yr during the younger period (Figure S 5). The modeled sediment accumulation rates agreed with 1963 (nuclear weapon tests) and 1986 (Chernobyl) peaks in ^{137}Cs and the thickness of preserved sediment lamination.

The inner fjord sediment core He560-26-2-K1 (22 cm long), collected from an area in Brepollen, that was deglaciated during the last 50 years (Figure 1), showed $^{210}Pb_{ex}$ throughout, indicating

recent rapid deposition. There was no clear depth trend in $^{210}Pb_{ex}$, and ^{137}Cs was present throughout. The calculated sediment accumulation rate was in the order of 25.5 mm/yr. $^{210}Pb_{sup}$ (^{226}Ra) measured via its daughter ^{214}Pb yielded an apparent cyclicity, which could be related to annual layering and respective accumulation rate in the order of 30 mm/yr. Thus, the core is considered to comprise deposits accumulated within the last decade (Figure S 6).

Geological units

Please use the following geological map of Hornsund fjord, Svalbard, by the polish academy of science created by Birkenmajer (1990)[10]:

http://geoinfo.amu.edu.pl/sgp/wgs04/01Hornsund/M%20geol%20Hornsundu-HI.jpg

It displays the outcropping geological units which supply the local fjord sediments by glacial erosion. They likely include low- to mid-grade coal seems, however, they are likely in minority and no outcrops are documented. Moreover, due to the extensive glacial cover in the study area, the subglacial geology may be only extrapolated from adjacent exposed areas further north.

Supplementary Table

Table S 1: Radiocarbon signature and respective ages of n-alkanes.

sample label	target comment	$F^{14}C$	±1σ	Age (^{14}C)	±1σ
HH14-897-GC-MF 0-3cm	*n*-C_{19}	0.016	0.006	33322	2675
HH14-897-GC-MF 0-3cm	*n*-C_{20}	0.006	0.005	40883	5038
HH14-897-GC-MF 0-3cm	*n*-C_{21}	0.010	0.006	36860	3774
HH14-897-GC-MF 0-3cm	*n*-C_{22}	0.006	0.007	40594	5885
HH14-897-GC-MF 0-3cm	*n*-$C_{26+28+30}$	0.017	0.005	32797	2050
HH14-897-GC-MF 0-3cm	*n*-$C_{27+29+31}$	0.051	0.005	23868	704
HH14-897-GC-MF 86-89cm	*n*-C_{19}	0.003	0.005	47332	8100
HH14-897-GC-MF 86-89cm	*n*-C_{20}	0.002	0.005	50688	10673
HH14-897-GC-MF 86-89cm	*n*-C_{21}	0.006	0.006	41041	5262
HH14-897-GC-MF 86-89cm	*n*-C_{22}	0.004	0.006	44650	7636
HH14-897-GC-MF 86-89cm	*n*-$C_{26+C28+C30}$	0.001	0.004	52331	10160
HH14-897-GC-MF 86-89cm	*n*-$C_{27+C29+C31}$	0.018	0.004	32387	1780
HH14-897-GC-MF 133-136cm	*n*-C_{19}	0.003	0.004	46486	6268
HH14-897-GC-MF 133-136cm	*n*-C_{20}	0.002	0.004	49049	7751
HH14-897-GC-MF 133-136cm	*n*-C_{21}	0.013	0.004	34871	2102
HH14-897-GC-MF 133-136cm	*n*-C_{22}	0.001	0.004	52805	11536
HH14-897-GC-MF 133-136cm	*n*-$C_{26+28+30}$	0.003	0.003	46920	6014
HH14-897-GC-MF 133-136cm	*n*-$C_{27+29+31}$	0.027	0.004	29063	1074

Table S 2: Core ID, location, water depth and associated cruise reports of the analyzed sediment cores.

Core ID	Latitude [N]	Longitude [E]	Water depth [m]	Reference
HH14-897-GC-MF	76°59.555’	016°24.313’	140	Forwick et al. 2014[11]
He519_2-3	76° 58,957'	015° 49,194'	202	Mark et al. 2018[12]
He560_26-2-K1	76° 59,520‘	016° 33,898‘	46	Mark et al. 2020[13]

Supplementary Figures

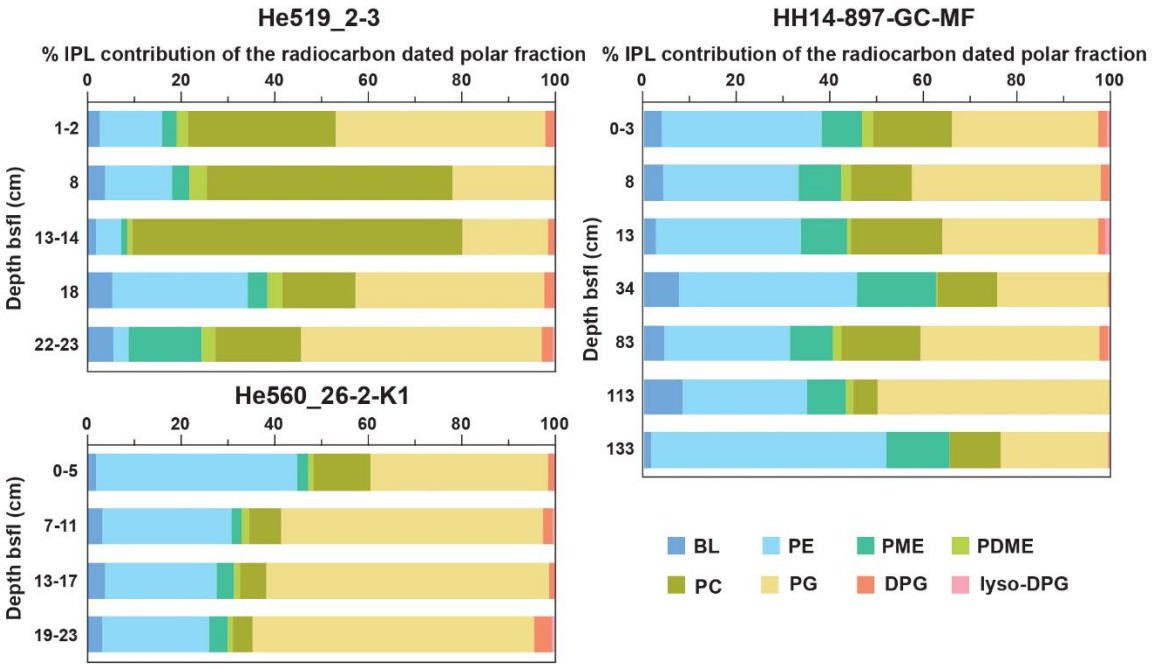

Figure S 1: Intact polar lipid distribution of the radiocarbon dated polar fraction with depth in the three analyzed cores. BL- betaine lipids, PE- phosphatidylethanolamine, PME- phosphatidyl-(N)-monomethylethanolamine, PDME- phosphatidyl-(N,N)-dimethylethanolamine (PDME), PC-phosphatidylcholine, PG- phosphatidylglycerol, DPG- diphosphatidylglycerol.

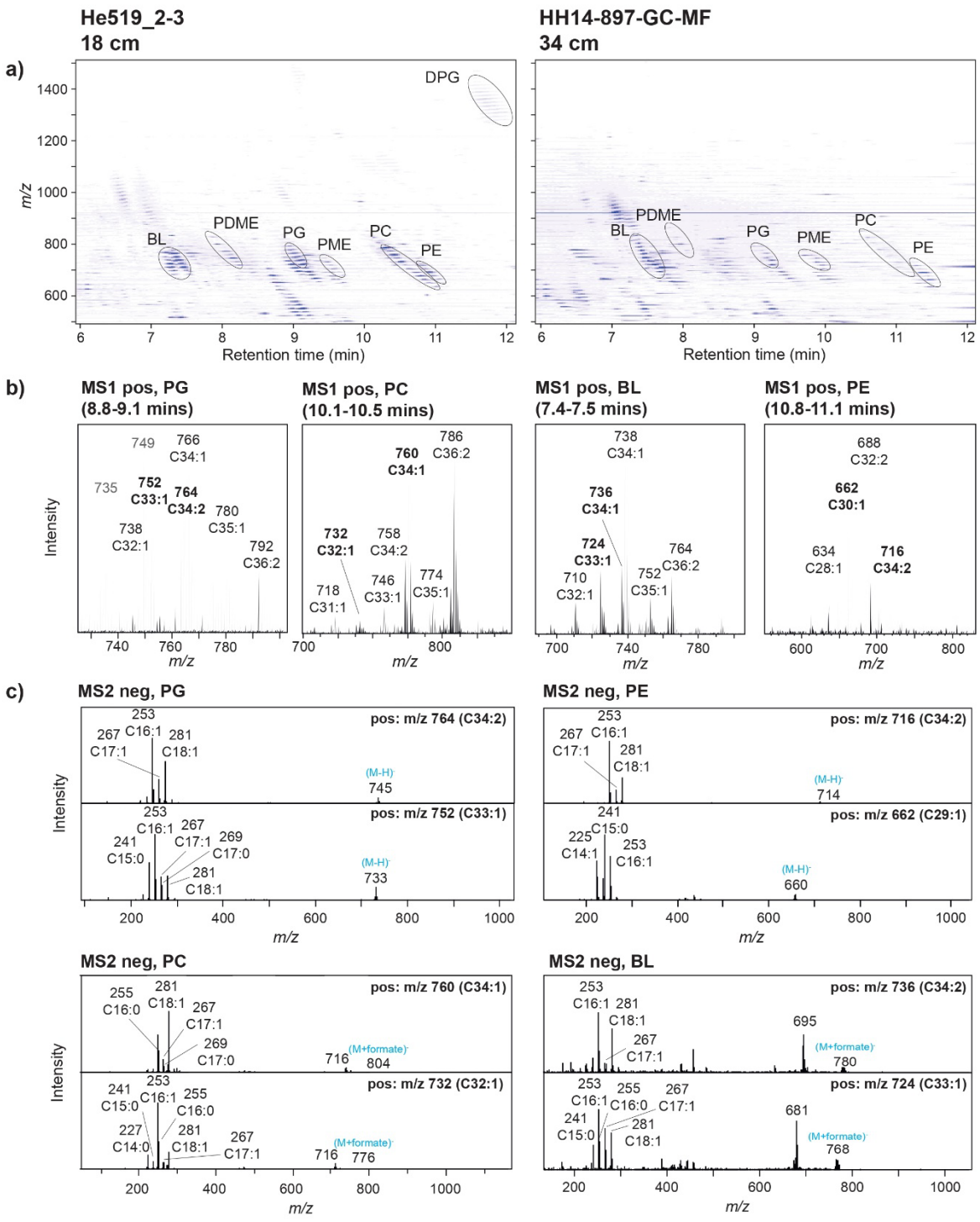

Figure S 2: a) Representative HPLC-MS chromatograms for the investigated sites depicted as heat maps showing the elution order of the detected phospholipids and amino lipids (zoom-in to retention time 6 to 12 min and m/z 550 to 1450) (for abbreviations see figure S 1). b) Distribution

of molecular ions in the MS1 in positive mode with the corresponding combined fatty acid chain length for betaine lipids and the most abundant phospholipids. c) Representative negative mode MS2 fragmentation patterns of betaine lipids and phospholipids marked in bold in panel b) showing the presence of the radiocarbon dated C16:1 and C15:0 fatty acids in all of the polar lipids.

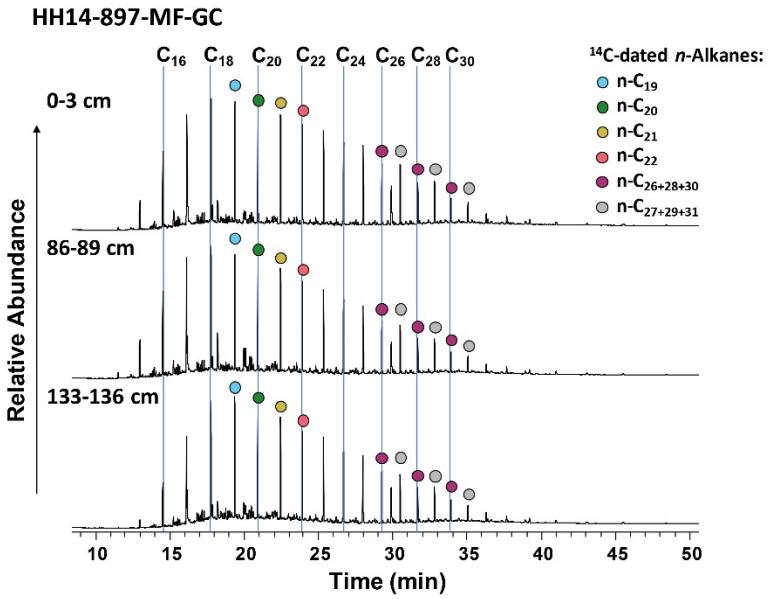

Figure S 3: Chromatograms for characteristic alkane distributions throughout the three cores displaying carbon preference index (CPI) values which indicate high (thermal) maturity (close to 1). The chromatograms shown here display the radiocarbon dated n-alkanes of the three depth intervals of sediment core HH14-897-GC-MF.

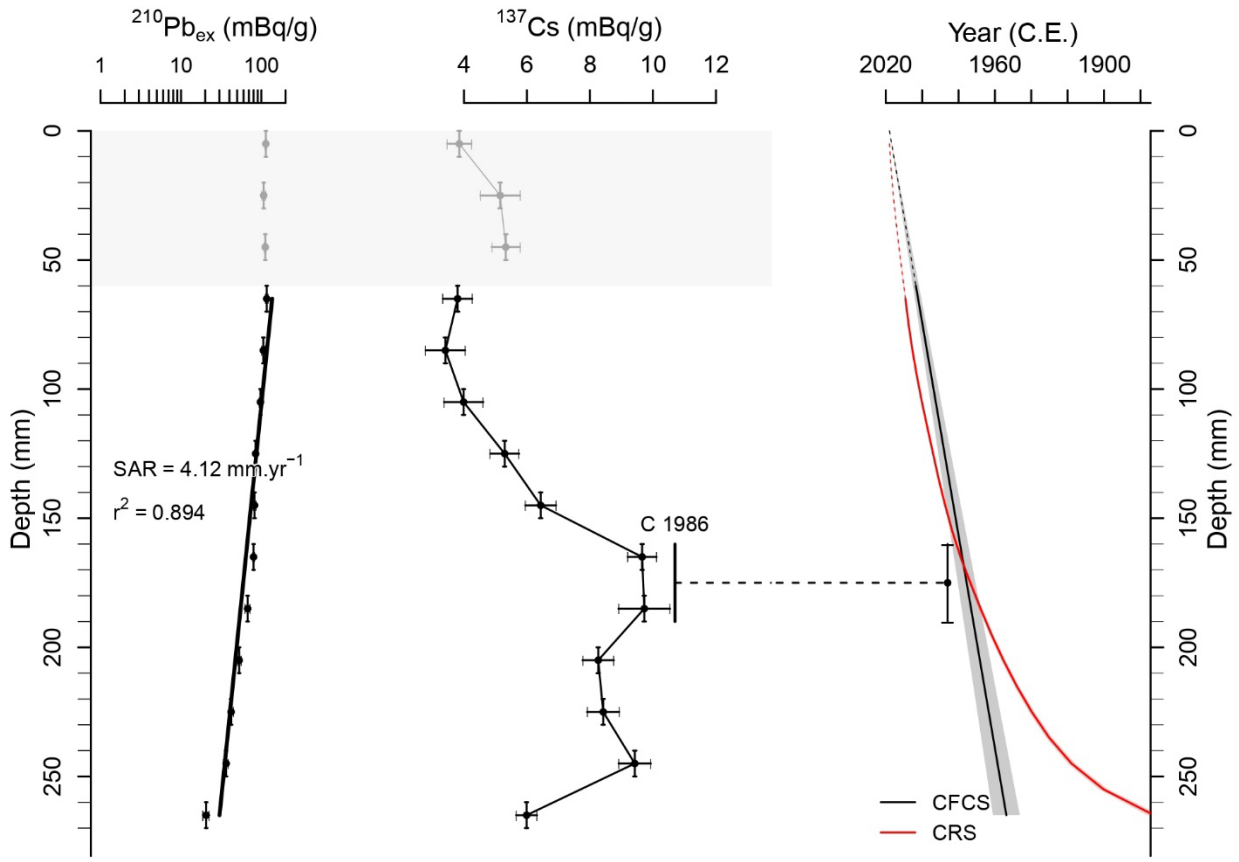

Figure S 4: Short-lived radionuclide measurements, and age depth model for He519_2-3 core. From left to right: $^{210}Pb_{ex}$ (semilogarithmic plot of excess ^{210}Pb), ^{137}Cs, the CFCS (constant flux constant sedimentation rate), and CRS (constant rate of supply) age models. SAR – sediment accumulation rate calculated with CFCS model, C 1986 – Chernobyl Nuclear Power Plant disaster in 1986. The surface mixed layer (SML) is in light gray (top 60 mm). Data are presented as mean values. The vertical error bars refer to analyzed sediment sample thickness, while the horizontal bars depict 1 SD uncertainties are based on decay counting statistics of individual samples (n=1) and include the error propagation from detector efficiency and background determinations. Uncertainties for the age model are calculated from the propagated 1 SD counting uncertainties

of the individual samples. The uncertainty resulting from model assumptions is not considered by error bars, but by comparison of different age models. The figure was created in serac R package[14].

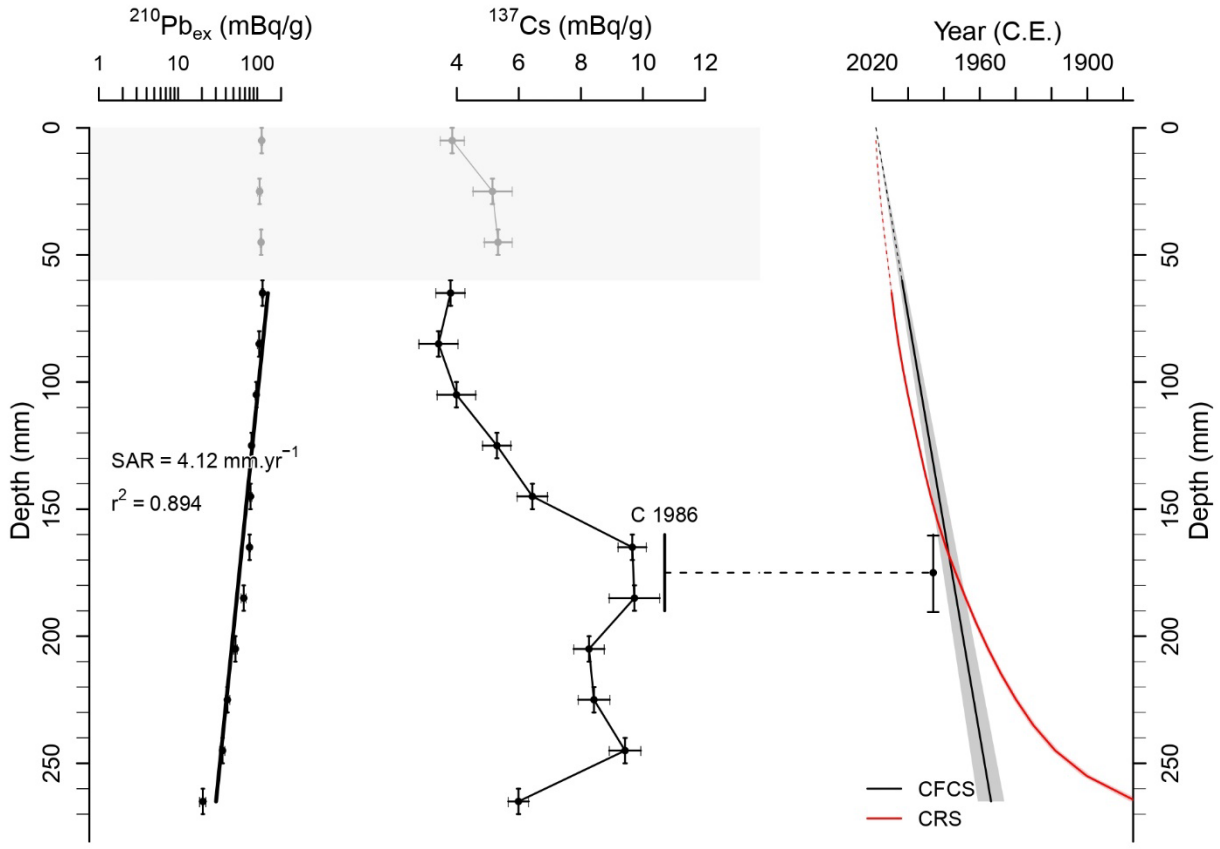

Figure S 5: Short-lived radionuclides measurements and age depth model for HH14-897-GC-MF core. From left to right: $^{210}Pb_{ex}$ (semilogarithmic plot of excess ^{210}Pb), ^{137}Cs, and the CFCS (constant flux constant sedimentation rate) with assumption of two periods of various accumulation rate, and CIC (constant initial concentration) age model. SAR – sediment accumulation rate calculated with CFCS model, C 1986 – Chernobyl Nuclear Power Plant disaster in 1986, NWT 1963 – Nuclear Weapon Tests fallout maximum in 1963. The coring site was deglaciated after 1920[15]*. Data are*

presented as mean values. The vertical error bars refer to analyzed sediment sample thickness, while the horizontal bars depict 2 SD uncertainties are based on decay counting statistics of individual samples (n=1) and include the error propagation from detector efficiency and background determinations. Uncertainties for the age model are calculated from the propagated 2 SD counting uncertainties of the individual samples. The uncertainty resulting from model assumptions is not considered by error bars, but by comparison of different age models. The figure was created in serac R package[14].

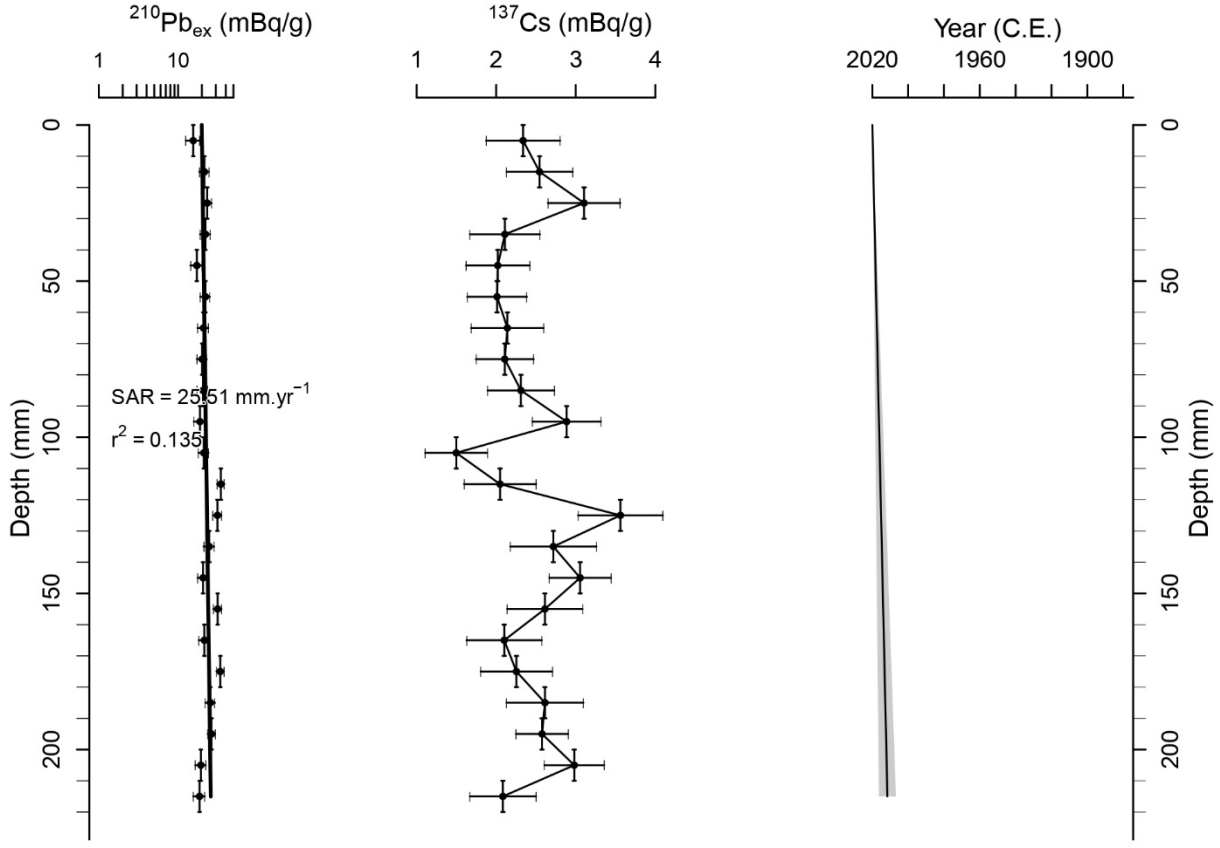

Figure S 6: Short-lived radionuclides measurements and age depth model for He560_26-2-K1 core. From left to right: $^{210}Pb_{ex}$ (semilogarithmic plot of excess ^{210}Pb), ^{137}Cs, and the CFCS (constant flux

constant sedimentation rate) age model. SAR – sediment accumulation rate. Data are presented as mean values. The vertical error bars refer to analyzed sediment sample thickness, while the horizontal bars depict 1 SD uncertainties are based on decay counting statistics of individual samples (n=1) and include the error propagation from detector efficiency and background determinations. Uncertainties for the age model are calculated from the propagated 1 SD counting uncertainties of the individual samples. The uncertainty resulting from model assumptions is not considered by error bars, but by comparison of different age models. The figure was created in serac R package[14].

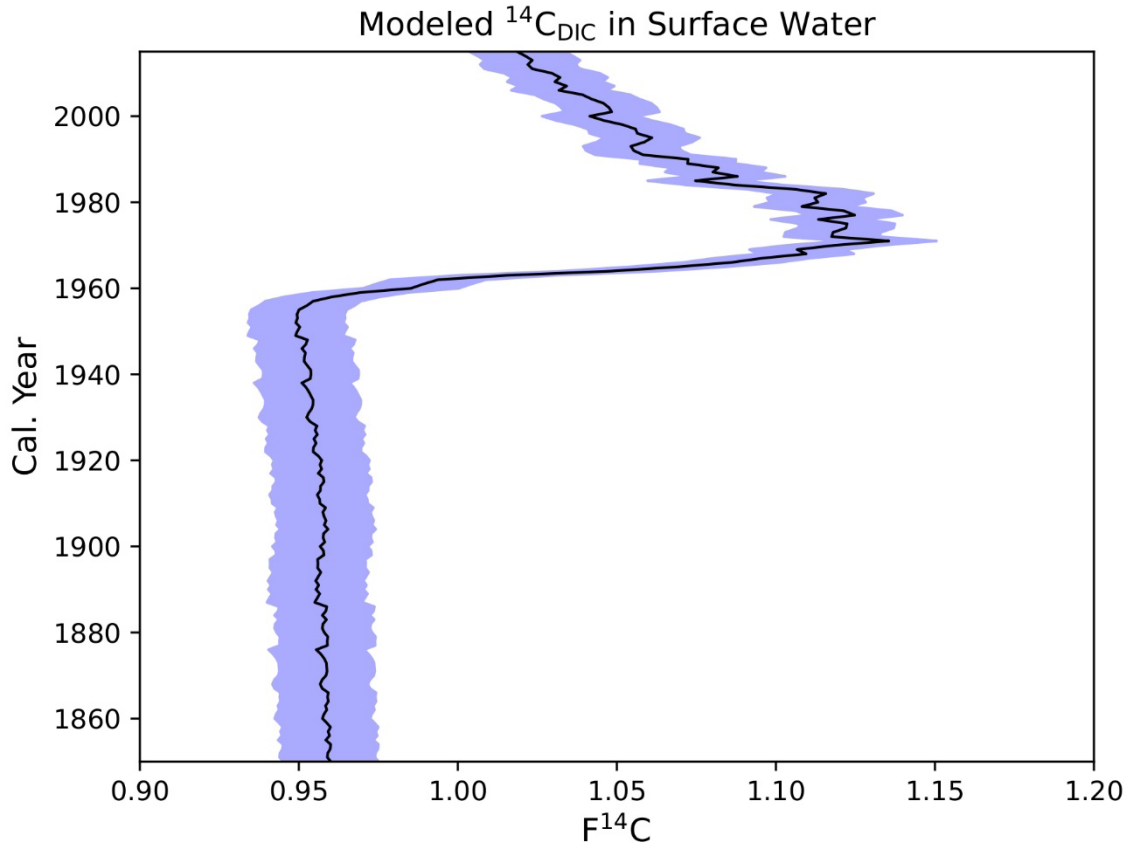

Figure S 7: History of dissolved inorganic radiocarbon ($F^{14}C$) near Hornsund according to a simulation with the FESOM2 model (see methods). Data are presented as mean values. Shading ($F^{14}C$ +-0.015) indicates the spatial variation of adjacent model results..

.

References

1. Sohlenkamp, C. & Geiger, O. Bacterial membrane lipids: diversity in structures and pathways. *FEMS Microbiol Rev* **40**, 133–159 (2016).

2. Lipp, J. S. & Hinrichs, K. U. Structural diversity and fate of intact polar lipids in marine sediments. *Geochim. Cosmochim. Acta* **73**, 6816–6833 (2009).

3. Schubotz, F. *et al.* Petroleum degradation and associated microbial signatures at the Chapopote asphalt volcano, Southern Gulf of Mexico. *Geochim. Cosmochim. Acta* **75**, 4377–4398 (2011).

4. Sohlenkamp, C. *et al.* Biosynthesis of phosphatidylcholine in bacteria. *Prog. Lipid Res.* **42**, 115–162 (2003).

5. Dembitsky, V. M. Betaine ether-linked glycerolipids: Chemistry and biology. *Prog. Lipid Res.* **35**, 1–51 (1996).

6. Harvey, H. R. *et al.* The effect of organic matter and oxygen on the degradation of bacterial membrane lipids in marine sediments. *Geochim. Cosmochim. Acta* **50**, 795–804

(1986).

7. Logemann, J. *et al.* A laboratory experiment of intact polar lipid degradation in sandy sediments. *Biogeosciences* **8**, 2547–2560 (2011).

8. Bianchi, T. S. & Canuel, E. A. *Chemical biomarkers in aquatic ecosystems*. (Princeton University Press, 2011).

9. Mollenhauer, G. *et al.* Standard operation procedures and performance of the MICADAS radiocarbon laboratory at Alfred Wegener Institute (AWI), Germany. *Nucl. Instruments Methods Phys. Res. Sect. B Beam Interact. with Mater. Atoms* **496**, 45–51 (2021).

10. Birkenmajer, K. Geology of the Hornsund area, Spitsbergen. *Katowice, Pol.* **1**, 1–42 (1990).

11. Forwick, M. *et al. Cruise report: Marine-geological cruise to Hornsund, Svalbard*. (2014).

12. Mark, F. C. *et al. Cruise Report RV Heincke HE519*. (2018).

13. Mark, F. C. *HEINCKE-Berichte: Influence of climate change on interactions and biodiversity in Arctic ecosystems. Cruise No. HE 560*. (2020).

14. Bruel, R. & Sabatier, P. serac: an R package for ShortlivEd RAdionuclide chronology of recent sediment cores. *J. Environ. Radioact.* **225**, 106449 (2020).

15. Błaszczyk, M. *et al.* Fluctuations of tidewater glaciers in Hornsund Fjord (Southern Svalbard) since the beginning of the 20th century. *Polish Polar Res.* **34**, 327–352 (2013).